

Practical Driving Electronics for an AOTF-Based NO₂ Camera

Jurgen Vanhamel¹, Graduate Student Member, IEEE, Sophie Berkenbosch, Emmanuel Dekemper, Paul Leroux, Senior Member, IEEE, Eddy Neefs, and Emmanuel Van Lil, Senior Member, IEEE

Abstract—The measurement of NO₂ abundance in the air is of interest for monitoring pollution sources and air quality. A new instrumental concept has been recently introduced, which makes use of an acoustooptical tunable filter (AOTF) as the main component of a spectral imager. With the capability of resolving the absorption spectrum of NO₂, and a high spatial and temporal sampling, this instrument can be seen as a NO₂ camera. In this instrument, the selection of different optical wavelengths by the AOTF is done by applying a radio frequency (RF) signal to the AOTF. The selected frequency and the applied amplitude are the key parameters for the quality of the measurements. The design and assembly of an RF chain, consisting of an RF generator and RF amplifier, will lead to an electronics bench capable of driving the NO₂ camera. In view of a potential spaceborne application of this instrumental concept, the design of the RF generator is only making use of space-qualified components. This paper focuses on the development of this part of the electronics bench.

Index Terms—Acoustooptical tunable filter (AOTF), imaging system, NO₂, phase-locked loop (PLL), radio frequency (RF), spectroscopy.

I. INTRODUCTION

NITROGEN dioxide (NO₂) forms in combustion reactions, such as the ones taking place in vehicles' engines, oil firing heating systems, or coal and oil firing power plants. Due to its relatively long lifetime in the air, and because of its harmful effects on respiration [1], it is a key species to air quality. In urban areas, air pollution is traditionally sampled and monitored by networks of air analyzers. However, these networks, although valuable for triggering pollution alerts, provide too much localized information to grasp the global picture of the air pollution at the city scale. On the other side,

space-borne air quality sensors of the latest generation [e.g., European Space Agency (ESA) Sentinel-5P mission] still do not achieve the necessary spatial sampling either. To a large extent, the question of how to best monitor urban air pollution remains open.

Apart from densifying the current air analyzers networks, another approach is to rely on remote sensing instruments. So far, most of these instruments have been relying on grating spectrometers offering a high accuracy but a limited spatial resolution [2]. In order to improve on this aspect, a new type of remote sensing instrument has been developed. It is a spectral imager based on an acoustooptical tunable filter (AOTF) that is efficient at detecting the distribution of NO₂ with a high spatial and temporal resolution. Applying an AOTF in a spectrometer is a technique already used before [3], but also other applications are feasible [4].

The instrument principle and its application to the measurement of the NO₂ plume released by a coal-burning power plant have been described in Dekemper 2016 [5].

The development of this instrument originates from the ESA atmospheric limb tracker for the investigation of the upcoming stratosphere (ALTIUS) mission [6], [7]. This mission has the aim to measure atmospheric trace species concentration profiles with a high spatial resolution. Three independent channels will be responsible for the acquisition of spectral images of the bright atmospheric limb at specific wavelengths in different spectral ranges, namely, ultraviolet (from 250 to 400 nm), visible (from 440 to 800 nm), and near infrared (from 900 to 1800 nm). The visible channel was breadboarded at an early stage of the project [8] using a TeO₂ AOTF and served as the basic idea for the NO₂ monitoring instrument. Several adaptations are introduced compared to the previously designed ALTIUS visible channel breadboard. The used spectral range is reduced to 430–470 nm, the used camera is changed from a mechanical shutter principle to a CMOS-based design, the applied steering electronics are changed, and the total length of the instrument is reduced. The aim is to translate this ground-based instrument into a space-based payload on board a spacecraft platform in a later stage. For this reason, the used electronics has to be in line with approved, qualified, and available space grade components.

The purpose of this paper is to clarify, from a technical point of view, the working principle of the instrument and more specifically the driving electronics as a whole and the phase-locked loop (PLL) radio frequency (RF) generator in particular.

Manuscript received March 21, 2018; revised May 25, 2018; accepted June 18, 2018. Date of publication August 1, 2018; date of current version February 8, 2019. This work was supported in part by the Department of Engineering and the Department of Solar Radiation in Atmospheres of the Royal Belgian Institute for Space Aeronomy and in part by PRODEX under Contract 4000110400. The Associate Editor coordinating the review process was Dr. George Xiao. (Corresponding author: Jurgen Vanhamel.)

J. Vanhamel, S. Berkenbosch, E. Dekemper, and E. Neefs are with the Royal Belgian Institute for Space Aeronomy, 1180 Brussels, Belgium (e-mail: jurgen.vanhamel@aeronmie.be; sophie.berkenbosch@aeronmie.be; emmanuel.dekemper@aeronmie.be; eddy.neefs@aeronmie.be).

P. Leroux is with the Advanced Integrated Sensing Lab, Department of Electrical Engineering (ESAT), KU Leuven, 3000 Leuven, Belgium (e-mail: paul.leroux@kuleuven.be).

E. Van Lil is with the Department of Electrical Engineering, Telecommunications and Microwaves (ESAT-TELEMIC), KU Leuven, 3001 Leuven, Belgium (e-mail: emmanuel.vanlil@kuleuven.be).

Color versions of one or more of the figures in this paper are available online at <http://ieeexplore.ieee.org>.

Digital Object Identifier 10.1109/TIM.2018.2853898

TABLE I
RF GENERATOR DESIGN PARAMETERS

Requirement	Value
Frequency Range	130 – 160 MHz
Unwanted spectral components in RF output	< -30 dBc
Nominal load	50 Ohm
RF generator accuracy	1 kHz
RF long term (10 s) frequency stability	5 kHz
Phase noise	< -120 dBc/Hz at 10 kHz
RF resolution	5 kHz
RF generator output power	> +3 dBm
RF output power at AOTF transducer side	100 mW (± 10%)
Stabilization time RF system	< 5 ms
RF output power uncertainty	1 mW

II. INSTRUMENT PERFORMANCE REQUIREMENTS AND GENERAL INSTRUMENT SETUP

During the design phase of the instrument, it became clear that the design would be constrained by practical and scientific requirements. Several design parameters were imposed each flown down from the scientific requirements. In Table I, the most prominent parameters are listed. In the following, the necessity of these parameters is discussed.

A. Portability

The instrument has to perform a full-day measurement on battery power, which automatically imposes a low power consumption. In addition, the setup has to be light and portable to reach remote measurement locations such as rooftops, volcanoes, and high mountain tops.

For the reason of portability and lightweight, the setup of the instrument consists of two parts: one part is known as the optical bench and the other contains the driving electronics (Fig. 1). Both benches are housed inside two separate boxes and combined onto a baseplate which can be mounted onto a tripod for azimuthal and elevational optical alignment of the observed scenery. The splitting of the instrument into two boxes originates from the avoidance of any heat transfer from the electrical toward the optical bench. Due to additional heat, the optical alignment of the instrument can be perturbed.

B. Optical Design

The imaging aspect of the instrument is one of the features that make it better adapted to capturing 2-D fields of NO₂ above cities or emission sites. The optical setup consists of a pupil and a lens to bundle the light into the AOTF which is surrounded by two polarizers. The first order of diffraction of the AOTF is collected by relay optics which eventually focuses the spectral image onto the CMOS detector. The undesired part of the optical spectrum is filtered out by the cross orientation of the polarizers and a beam stop.

C. Framerate

In order to leave as much time as possible to the signal integration at detector level, the tuning of the AOTF driving

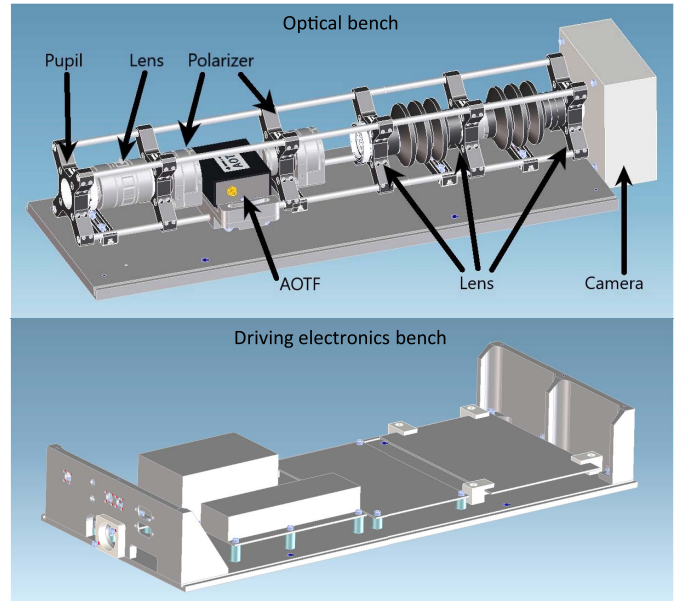


Fig. 1. Setup of the instrument (optical and electronic bench).

frequency was required to take less than 5 ms. A dedicated software was developed in order to orchestrate different steps of an image acquisition. The final frame rate depends on the scene luminosity, but the target is 10 Hz.

D. Tuning Range and Optical Wavelength Selection

The AOTF serves as a filter to select different optical wavelengths. The working principle of the AOTF is based on the interaction between sound and light inside a birefringent crystal [9], [10]. The applied RF signal is translated into an acoustic wave inside the crystal (made of TeO₂) by the use of a transducer. In addition, the acoustic wave interacts with the incoming light waves inside the crystal so that by momentum matching a narrow portion of the light diffracts in a different direction.

The AOTF used in this instrument is a commercial product from Gooch and Housego, which was described in detail in [5] and [8]. Its transparency domain ranges from 350 nm to 3.5 μ m. For the remote sensing of NO₂, most instruments select the region between 400 and 500 nm because the absorption by the molecule is the strongest and interference by ozone is at its lowest (see [5] for the absorption spectrum of NO₂ measured with this AOTF). For this NO₂ camera, we focused on the region 430–470 nm, which according to the laws of acoustooptics and for this particular AOTF, corresponds to acoustic frequencies ranging from 130 to 160 MHz.

The advantage of using an AOTF compared to a filter-based solution is that any optical wavelength within the given range can be selected simply by tuning the acoustic frequency. For our application, we needed an instrument capable of resolving the structures of the absorption cross section of NO₂. These structures are adequately sampled at 0.1 nm. The corresponding sampling in the frequency domain is given by the derivative of the tuning curve as in the following equation:

$$df = \lambda/f(\lambda) \cdot d\lambda. \quad (1)$$

For $\lambda = 450$ nm and $f = 150$ MHz, one obtains $df \approx 30$ kHz. Taking some safety margin on this number, the RF tuning step was required to be smaller than 5 kHz.

The accuracy of the RF tuning was required to be as small as 1 kHz, ensuring that the wavelength uncertainty would be much smaller than 0.1 nm.

A typical exposure time of 1 s is used for the imaging. Adding margin, the requirement of 5 kHz in a time interval of 10 s is taken as the RF long-term frequency stability. The 5-kHz value is based on (1) and on the wide bandwidth of 0.7 nm (or 200 kHz) of the AOTF. This also means that any phase noise appearing in the RF signal would not have any effect on the performed imaging.

E. RF Amplitude

The efficiency of the acousto-optic interaction can be controlled by the acoustic power sent into the crystal [10]. For this particular AOTF, and in the region around 450 nm, the optimal acoustic power should be around 100 mW. This value varies smoothly as a function of the wavelength. As it will be later explained, the analysis of the data always uses a normalization step either with some reference area in the image itself or with another image acquired at the same wavelength. Therefore, what really matters is the repeatability of the setting of the acoustic power in the crystal. An uncertainty of 1 mW is tolerated for the reproducibility of the driving power. In second position comes the achieved acoustic power, which is $100 \text{ mW} \pm 10\%$. With the latter requirement, one makes sure that most photons are indeed captured in the acousto-optic interaction.

F. Spectral Purity

The instrument design was made robust against RF generation harmonics by using an optical bandpass filter centered at 450 nm and delivering a bandwidth of 50 nm. By doing so, one makes sure that potential frequency harmonics will not find the corresponding photons in the AOTF, as they will be extinguished by the bandpass filter beforehand.

Other spurious frequencies are required not to reach an amplitude larger than -30 dBc, which guarantees that only the requested frequency has the necessary amplitude to drive the acousto-optic interaction. For this, the RF-zero power filter is implemented.

III. ELECTRONIC DRIVING SYSTEM

As mentioned earlier, an RF-driving mechanism is needed to make the birefringent crystal distinct between two optical beams. In general, this system is composed of an RF generator combined with an RF amplifier coupled to the transducer of the AOTF by an impedance matching network integrated into the AOTF housing (Fig. 2).

For the driving electronics bench, two RF generators are combined together with one RF amplifier to have a partially redundant system. One RF generator is based on the PLL, and the second is based on a commercial of the shelf direct digital synthesis-digital-to-analog convertor (DDS-DAC) principle.

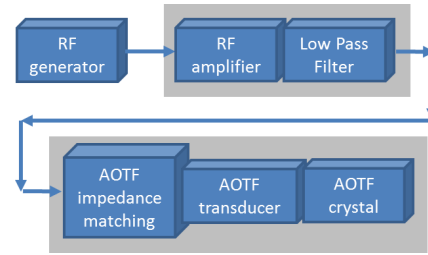


Fig. 2. General RF system overview.

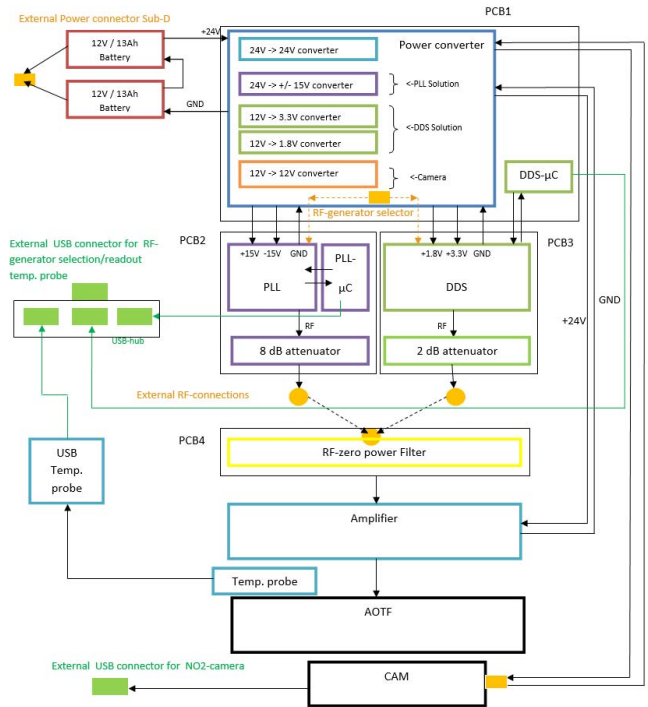


Fig. 3. Fully electrical design concept.

In Fig. 3, the full electrical design is shown. The PLL and DDS-DAC RF generator, together with a switching mechanism, the RF amplifier, the digital control devices, the temperature probe, and the voltage conversion are indicated on the block diagram.

The core of the driving system is printed circuit board (PCB) 2 and 3 containing the PLL and DDS-DAC RF generator, respectively. The possibility exists to switch between both RF generators. The output of the RF generators is attenuated to fulfill the allowable input power level of the minicircuits RF amplifier [11].

The signal enters a so-called “RF-zero power filter” (PCB 4). This filter is a third-order hourglass bandpass filter in which only the requested frequency range (130–160 MHz) is passed. The filter has a passband attenuation of 6 dB and a stopband attenuation of 20 dB. The attenuation obtained by using this passive filter is compensated by the output power of the RF generators. The RF amplifier increases the amplitude of the RF signal to 100 mW so that an optimum diffraction efficiency can be maintained in the AOTF. The temperature probe, mounted in the vicinity of the AOTF, monitors the ambient temperature during measurements so

that the temperature variation can be taken into account due to thermal drift in the AOTF. The universal serial bus (USB) driving of the microcontrollers for both RF generators, as well as the temperature probe readout, are all connected to a single chassis mounted USB connection at the outside of the electronic box. The power handling (PCB 1) is done by the use of several dc–dc converters, driving each electronic module in the system. The input voltage is a battery of 24-V dc, converted by the dc–dc converters to 1.8, 12, 15, –15, and 3.3 V.

IV. RF GENERATOR CONCEPTS

The generation of an RF-signal is a crucial part in the driving of the AOTF. For this, and testability reasons, two RF generators are implemented in the design to obtain redundancy. One generator is based on a PLL approach, and the other is based on a commercially available DDS-DAC AD9910 evaluation board [12].

As mentioned earlier, the idea is to translate this instrument into a possible future scientific space mission. This means that the used components have to have a space grade model available on the market. To select the appropriate RF generation technique, a tradeoff is performed between different RF generation techniques suitable for space applications such as single-side band mixing and PLL [13], [14]. Also, other possibilities were investigated such as repackaging of a commercial DDS-DAC chip into a space grade package, as well as using an application specific integrated circuit. Based on this tradeoff, the PLL-based RF generation technique came out as the best setup to be in line with low costs, agency (e.g., ESA) approved, qualified, and available on the market space grade components.

Notwithstanding this, two RF generators are implemented from a redundant as well as from a testability point of view. A long-term testing of the transferable space grade PLL RF generator can be performed and compared to the commercial implemented DDS-DAC RF generator. This latter is a commercial evaluation board and is built in the instrument as such. In this paper, only the PLL-based RF generator is discussed.

The design originates from a preliminarily designed RF generator for ALTIUS [15]. The used components are hence in line with space qualified components proposed in the preferred part list of ESA. Although this is less relevant for the proposed ground-based instrument, having space qualifiable setup gives a good starting point for a possible transfer of the instrument concept in a space mission.

The design of the PLL core consists of a space-qualified frequency synthesizer of analog devices (ADF4108) [16], in combination with a voltage-controlled oscillator (VCO) of minicircuits (ZX95-2500W+) [17] (Fig. 4). A custom-designed active loop filter is connected to the charge pump of the PLL. This filter is built around an operational amplifier of analog devices [18]. An active version is selected instead of a passive due to the requested high input voltage range of the VCO.

The output frequency of the VCO is too high for the requested frequency range, so two additional space-qualified dividers of Peregrine Semiconductor/E2V [19] are used.

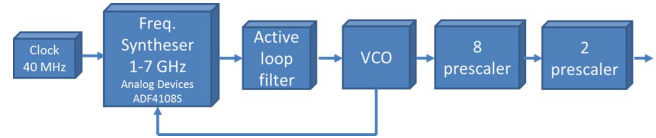


Fig. 4. PLL RF generator principle.

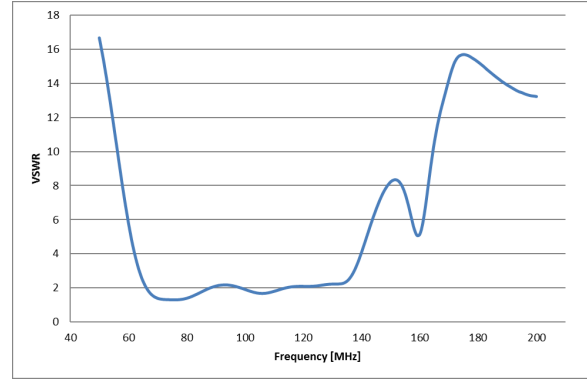


Fig. 5. Measured VSWR curve of the implemented AOTF.

By the use of an 8-bit Programmable Interrupt Controller microcontroller (PIC18F46J50) of Microchip [20], the PLL is controlled via the programmable frequency synthesizer.

V. MEASUREMENT RESULTS

To calibrate the final RF system different output power levels were measured at the transducer of the AOTF, taking into account the VSWR behavior of the transducer of the AOTF. This VSWR was measured (Fig. 5) and subsequently; the final output power of the amplifier was calculated.

In the next paragraph, the compliance with the design parameters (Table I) will be examined. The spectral output, resolution, phase noise, stability, and unwanted spectral component suppression of the used PLL RF generator concept are already investigated in [13]–[15]. Nevertheless, these measurements were redone on the current designed setup. As a summary, the measured values are given. The phase noise measured at 10-kHz offset is -101 dBc/Hz over the complete frequency range. Like stated earlier, this value has no effect on the performed NO₂ measurements. By programming the frequency synthesizer at different frequencies, a spectral output resolution of 5 kHz is achieved. The long-term frequency stability of the RF signal (5 kHz) is also within the requested limit of 10 s. The reference signal generates harmonics which are out of the range of the applied frequencies (130–160 MHz). The additional use of the RF-zero power filter (bandpass between 130 and 160 MHz) will remove the generated harmonics.

A. Stabilization Time

To achieve a high framerate, a quick switching between two frequencies is necessary. For this, the requirement of generating a stable RF output frequency has to be checked. The measurement starts from the moment a command “providing a specific frequency” is sent to the frequency synthesizer by the microcontroller. This is indicated as the start point (Fig. 6) from which the stabilization time is measured. The endpoint

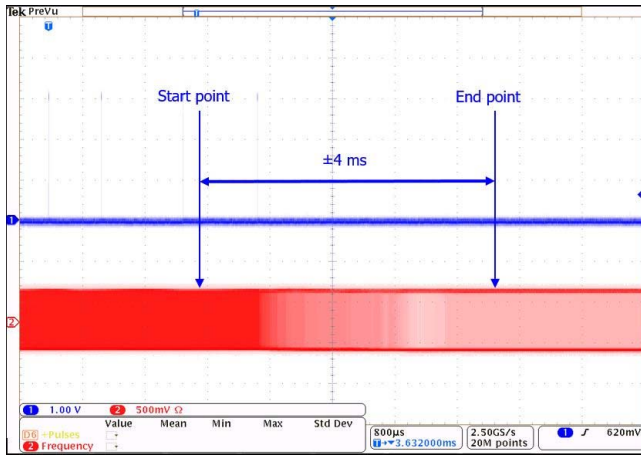


Fig. 6. Stabilization time switching from the highest to the lowest frequency.

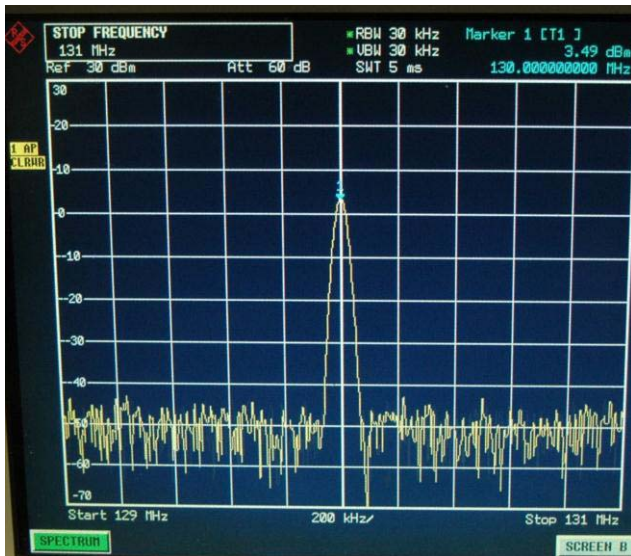


Fig. 7. Output power level RF generator at 130 MHz.

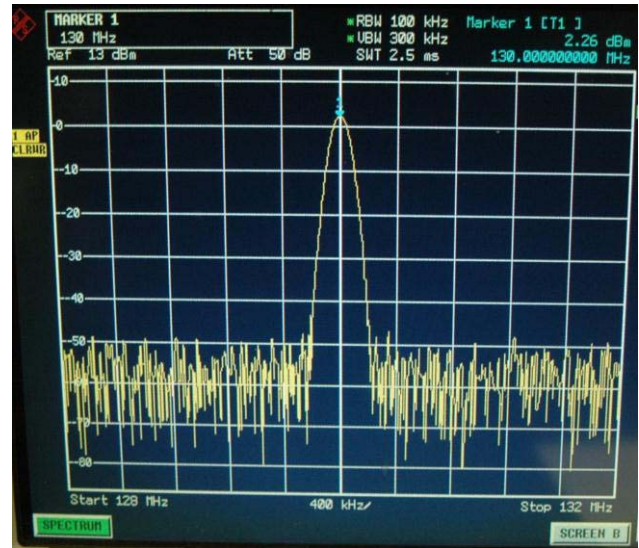


Fig. 8. Output power level RF amplifier at 130 MHz.

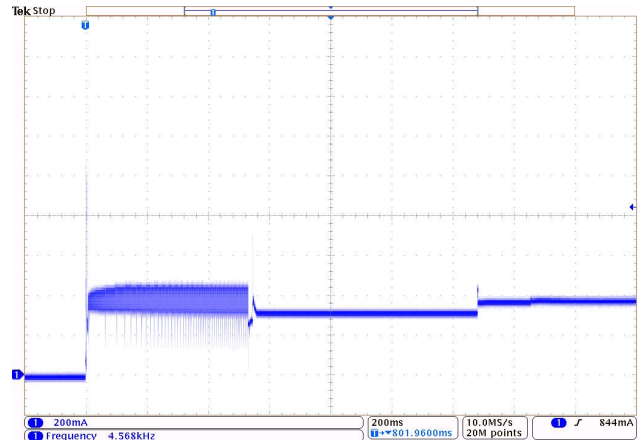


Fig. 9. Camera current peak at initial startup.

indicates the point where the RF generator has a stable output frequency. Adding some margin, the results show that around 4 ms are needed to have a stable signal, after switching from the highest to the lowest frequency. The software which drives the switching of the frequencies takes an additional 1-ms tolerance. By this, the requirement of 5 ms is fulfilled.

B. Output Level

The final requested output power at the transducer of the AOTF is set at 100-mW fix for the complete frequency range. A tolerance of 10% is allowed. The attenuation imposed by the VSWR of the transducer has to be taken into account. Measurements have been carried out to check the output level of the RF system as a whole. For this, the RF generator output power is measured at different frequencies. In addition, the RF amplifier is coupled to the RF generator, and the same measurements are performed.

In Fig. 7, for example, the output level of the RF generator at 130 MHz is shown and is at +3.5 dBm.

This output value is attenuated by 5.5 dB due to the use of the RF-zero power filter. In addition, an 8-dB attenuator is

used before entering the RF amplifier to achieve the requested output power level. The output power after the RF amplifier can be seen in Fig. 8 and is at +22.3 dBm. The vertical scale of Fig. 8 is offset by the 20 dB of the attenuator inserted at the entrance of the spectrum analyzer.

This is the final value needed to compensate for the VSWR behavior of the transducer, the cable length between the electronics bench and the attenuation due to the used connectors in the RF path.

The same measurements are done at different frequencies.

C. Peak Current Measurements

In the frame of the selection of applicable dc–dc convertors and batteries, the peak current of different submodules had to be investigated. Especially, the peak current of the high power consuming submodules, i.e., the camera and RF amplifier, were measured.

The initial startup of the camera imposes a relatively high current peak after which it stabilizes around 600 mA (Fig. 9).

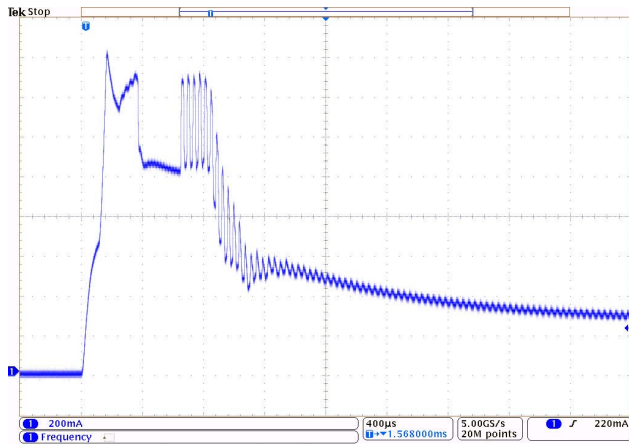


Fig. 10. RF amplifier current consumption at startup.

Fig. 11. NO₂ cell placed in the observed scene.

For the RF amplifier around 1.8 A is consumed at startup after which the level declines to a more acceptable level of 500 mA (Fig. 10).

D. RF Output Power Uncertainty

As explained earlier, the applied RF power toward the AOTF can have a maximum uncertainty of 1 mW in order to use the normalization step in the data analysis. By applying a dedicated power meter and performing several tests at different frequencies and time intervals, the variation of the output power was measured. No exceedance of 1 mW was detected.

E. Scientific Data

In order to illustrate the principle of the instrument, we pointed the NO₂ camera outside of the author's office and inserted in the camera field of view a glass cell containing a given concentration of NO₂ (Fig. 11). The control software was operated such that spectral images of this scene were acquired successively by steps of 0.1 nm from 445 to 455 nm. For each image, the exposure time was set to 4.5 s.

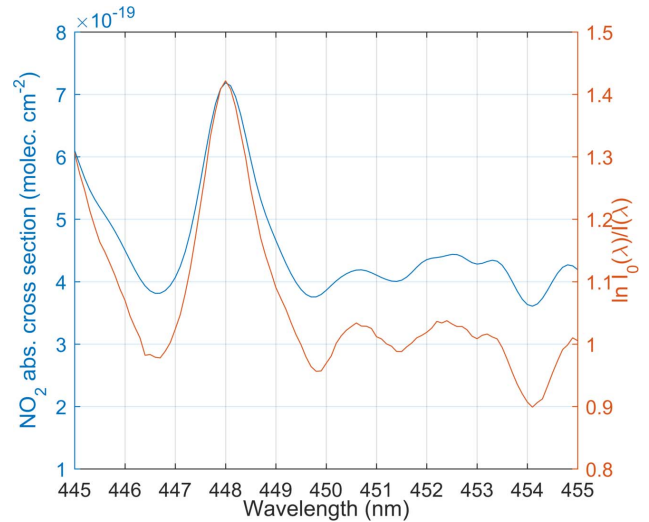


Fig. 12. Optical thickness and cross section comparison.

The Beer–Lambert extinction law (2) predicts that the transmission of the glass cell ($I(\lambda)$) varies exponentially as a function of the optical thickness encountered by the light

$$I(\lambda) = I_0(\lambda) \cdot \exp[-\tau_{\text{no}_2}(\lambda)]. \quad (2)$$

The optical thickness $\tau_{\text{no}_2}(\lambda)$ caused by the NO₂ contained in the cell depends on the concentration of NO₂ (n_{no_2}), the length of the cell (d), and the absorption cross section of a molecule of NO₂ [$\sigma_{\text{no}_2}(\lambda)$] given as [21]

$$\tau_{\text{no}_2}(\lambda) = \sigma_{\text{no}_2}(\lambda) \cdot n_{\text{no}_2} \cdot d. \quad (3)$$

This optical thickness is measured directly from the spectral images by taking the natural logarithm of the ratio of intensities seen inside $I_0(\lambda)$ and outside of the cell $I(\lambda)$ given as

$$\tau_{\text{no}_2}(\lambda) = \ln(I_0(\lambda)/I(\lambda)). \quad (4)$$

Fig. 12 compares the shape of the measured optical thickness of the cell (bottom curve) with the NO₂ absorption cross section (top curve) convolved to the instrument spectral resolution (approximately 0.6 nm). Clearly, the measured optical thickness spectrum is almost completely determined by the NO₂ absorption features, such that retrieving the abundance in the cell is straightforward.

VI. CONCLUSION

The discussed instrument, capable of imaging NO₂ fields, consists of two parts: an optical bench and an electronic driving bench. The steering of the optical bench by using the electronic driving mechanism is presented in this paper. More specifically, the PLL RF generator is highlighted. The development of a PLL RF generator for the ALTIUS ESA space mission is taken as a baseline for this instrument. Having the possibility of converting the used PLL RF generator concept into space qualified generator can lead to a possible space instrument. This can be the subject of the future research.

ACKNOWLEDGMENT

The authors would like to thank the Engineering and Solar Radiation Department for their performed work.

REFERENCES

- [1] M. Kampa and E. Castanas, "Human health effects of air pollution," *Environ. Pollution*, vol. 151, no. 2, pp. 362–367, Jan. 2008, doi: [10.1016/j.envpol.2007.06.012](https://doi.org/10.1016/j.envpol.2007.06.012).
- [2] G. Hönninger, C. von Friedeburg, and U. Platt, "Multi axis differential optical absorption spectroscopy (MAX-DOAS)," *Atmos. Chem. Phys.*, vol. 4, no. 1, pp. 231–254, 2004, doi: [10.5194/acp-4-231-2004](https://doi.org/10.5194/acp-4-231-2004).
- [3] A. N. Mortensen, S. A. Dyer, R. M. Hammaker, and W. G. Fateley, "A Hadamard-multiplexed spectrometer based on an acousto-optic tunable filter," *IEEE Trans. Instrum. Meas.*, vol. 45, no. 2, pp. 394–398, Apr. 1996.
- [4] H. Takahashi, C. Masuda, Y. Gotoh, and J. Koyama, "Laser diode interferometer for vibration and sound pressure measurements," *IEEE Trans. Instrum. Meas.*, vol. 38, no. 2, pp. 584–587, Apr. 1989.
- [5] E. Dekemper, J. Vanhamel, B. V. Opstal, and D. Fussen, "The AOTF-based NO₂ camera," *Atmos. Meas. Techn.*, vol. 9, no. 12, pp. 6025–6034, 2016.
- [6] D. Fussen *et al.*, "The ALTIUS mission," *Atmos. Meas. Tech. Discuss.*, pp. 1–40, 2016, doi: [10.5194/amt-2016-213](https://doi.org/10.5194/amt-2016-213).
- [7] E. Dekemper *et al.*, "ALTIUS: A spaceborne AOTF-based UV-VIS-NIR hyperspectral imager for atmospheric remote sensing," *Proc. SPIE*, vol. 9241, pp. 92410L-1–92410L-10, Oct. 2014.
- [8] E. Dekemper *et al.*, "Tunable acousto-optic spectral imager for atmospheric composition measurements in the visible spectral domain," *Appl. Opt.*, vol. 51, no. 25, pp. 6259–6267, 2012.
- [9] I. C. Change, "Noncollinear acousto-optic filter with large angular aperture," *Appl. Phys. Lett.*, vol. 25, no. 7, pp. 370–372, 1974, doi: [10.1063/1.1655512](https://doi.org/10.1063/1.1655512).
- [10] E. Dekemper, "Development of an AOTF-based hyperspectral imager for atmospheric remote sensing," Ph.D. dissertation, Inst. Condensed Matter Nanosci., Nanoscopic Phys., Univ. Catholique de Louvain, Louvain-la-Neuve, Belgium, 2014, pp. 99–136.
- [11] Minicircuits. *ZHL-2-8+*, *Datasheet*. Accessed: Jan. 15, 2018. [Online]. Available: <https://www.minicircuits.com/pdfs/ZHL-2-8+.pdf>
- [12] Analog Devices. *DDS-DAC EVAL-AD9910 Evaluation Board*. Accessed: Jan. 17, 2018. [Online]. Available: <http://www.analog.com/en/design-center/evaluation-hardware-and-software/evaluation-boards-kits/eval-ad9910.html>
- [13] J. Vanhamel *et al.*, "RF-driving of acoustic-optical tunable filters; design, realization and qualification of analog and digital modules for ESA," *Microelectron. Rel.*, vol. 55, nos. 9–10, pp. 2103–2107, 2015, doi: [10.1016/j.microrel.2015.07.034](https://doi.org/10.1016/j.microrel.2015.07.034).
- [14] J. Vanhamel *et al.*, "Implementation of different RF-chains to drive acousto-optical tunable filters in the framework of an ESA space mission," *URSI Radio Sci. Bull.*, vol. 2016, no. 357, pp. 37–43, Jun. 2016, doi: [10.23919/URSIRSB.2016.7909803](https://doi.org/10.23919/URSIRSB.2016.7909803).
- [15] J. Vanhamel, S. Berkenbosch, E. Dekemper, P. Leroux, E. Neefs, and E. Van Lil, "Testing of a possible RF-generator for a space based AOTF application in the frame of an ESA space mission," presented at the Int. Union Radio Sci. Gen. Assem. Sci. Symp., Montreal, QC, Canada, Aug. 2017, doi: [10.23919/URSIGASS.2017.8105079](https://doi.org/10.23919/URSIGASS.2017.8105079).
- [16] Analog Devices. *ADF4108*, *Datasheet*. Accessed: Jan. 10, 2018. [Online]. Available: <http://www.analog.com/en/products/rf-microwave/pll-synth/integer-n-plls/adf4108.html>
- [17] Minicircuits. *VCO ZX95-2500W+*, *Datasheet*. Accessed: Jan. 10, 2018. [Online]. Available: <http://194.75.38.69/pdfs/ZX95-2500W+.pdf>
- [18] Analog Devices. *AD820*, *Datasheet*. Accessed: Jan. 12, 2018. [Online]. Available: www.analog.com/media/en/technical-documentation/datasheets/AD820.pdf
- [19] E/Peregrine. *Space Qualified Prescalers*, *Datasheet*. Accessed: Jan. 20, 2018. [Online]. Available: <http://www.e2v-us.com/products/semiconductors/peregriner/f/>
- [20] Microchip. *PIC18F46J50 8-Bit Microcontroller*, *Datasheet*. Accessed: Feb. 2, 2018. [Online]. Available: <http://www.microchip.com/wwwproducts/en/PIC18F46J50>
- [21] A. C. Vandaele *et al.*, "High-resolution Fourier transform measurement of the NO₂ visible and near-infrared absorption cross sections: Temperature and pressure effects," *J. Geophys. Res.*, vol. 107, no. D18, pp. ACH3-1–ACH3-12, 2002.



Jurgen Vanhamel (GS'18) was born in Hasselt, Belgium, in 1978. He received the bachelor's degree in mathematics from KHLim, Hasselt, in 1999, the M.Sc. degree in industrial sciences, electronics, option information, and communication technology from PXL-XIOS, Diepenbeek, Belgium, in 2003, and the postgraduate degree in avionics and spaceionics from KHBO, Oostende, Belgium, in 2011. He is currently pursuing the Ph.D. degree with the Faculty of Engineering Technology, KU Leuven, Leuven, Belgium.

He was a Project Engineer with the Belgian Institute for Space Aeronomy, Brussels, Belgium, where he is involved in space mission called ALTIUS and also several other ground-based projects.

Sophie Berkenbosch received the M.Sc. degree in industrial engineering, electronics, option design technique from the KAHO Sint Lieven Department, KIH0, Gent, Belgium, in 2000.

She has contributed to designing, building, and operating ground-based scientific instrumentation as well as space instruments on several European Space Agency missions such as THOR, ALTIUS, ExoMars TGO, BepiColombo, SOIR, and NOMAD, specifically, in the following two scientific domains: *in situ* mass spectrometry and remote optical spectroscopy. The primary tasks accomplished as a project engineer included: design and implementation of space hardware, firmware, and software components, functional and environmental qualification and acceptance testing, design and implementation of ground support systems, and data archiving. Since 2011, she has been the Head of the Electronics Lab, Royal Belgian Institute for Space Aeronomy, Brussels, Belgium.



Emmanuel Dekemper received the Ph.D. degree in physics from the Université Catholique de Louvain, Ottignies-Louvain-la-Neuve, Belgium.

He has been with the Belgian Institute for Space Aeronomy, Brussels, Belgium. He is involved in the development of space-borne and ground-based remote sensing instruments for atmospheric composition measurement. His current research interests include the development of new instrumental concepts and retrieval algorithms



Paul Leroux (S'99–M'04–SM'10) was born in Eeklo, Belgium, in 1975. He received the M.Sc. and Ph.D. degrees in electronic engineering from the KU Leuven (University of Leuven), Leuven, Belgium, in 1999 and 2004, respectively.

From 1999 to 2004, he was a Teaching and Research Assistant with the MICAS Research Group, Department of Electrical Engineering (ESAT), KU Leuven, where he became a Professor in 2009 and he was the Head of the Electrical Engineering (ESAT) Technology Cluster from 2011 to 2016. Since 2016, he has been the Campus Chair of KU Leuven, Geel, Belgium. He was with the ADVISE Research Group, Geel, where he was involved in radiation hardened analog and mixed-signal IC design for communication and instrumentation in space, high-energy physics, and nuclear energy applications. His group is part of the CERN CMS collaboration where he is acting as the KU Leuven Team Leader. He has co-authored over 150 papers in international journals and conference proceedings.

Dr. Leroux was a recipient of the SCK-CEN Prof. Roger Van Geen Award from the FWO and FNRS for his highly innovative work on IC design for harsh radiation environments in 2010.



Eddy Neefs was born in 1965. He received the M.Sc. degree in electronic engineering and the Ph.D. degree in applied sciences from KU Leuven (University of Leuven), Leuven, Belgium, in 1988 and 1996, respectively.

From 1988 to 1989, he was with the Royal Observatory of Belgium, Ukkel, Belgium, where he was involved in global positioning systems. In 1988, he joined the Royal Belgian Institute for Space Aeronomy, Ukkel, as a Project Engineer, where he was involved in the development of scientific instruments

related to optical and mass spectrometry. He was involved in many scientific space missions such as SPICAM, ROSINA, SPICAV, NOMAD, and ALTIUS, and also contributed to stratospheric balloon experiments. Since 2006, he has been with the Head of the Engineering Department, Royal Belgian Institute for Space Aeronomy.



Emmanuel Van Lil (S'74–M'81–SM'03) received the M.Sc., Ph.D., and special dr. degrees from KU Leuven, Leuven, Belgium, in 1977, 1983, and 1991, respectively.

Until 1983, he investigated the optimization of microstrip antenna arrays. He was a Visiting Scientist with the University of Houston, Houston, TX, USA, and the New York Polytechnic Institute, New York City, NY, USA. He implemented a near-field chamber and developed components for civilian radars. Since 1991, he has been focused on adaptive

antennas, propagation effects, and mobile telecommunication networks. He teaches wireless telecommunication systems, propagation, satellite communications, and avionics.